Optics Letters

Three-dimensional, multi-wavelength beam formation with integrated metasurface optics for Sr laser cooling

Sɪɴᴅʜᴜ Jᴀᴍᴍɪ,[1,2] Aɴᴅʀᴇᴡ R. Fᴇʀᴅɪɴᴀɴᴅ,[1,2] Zʜᴇɴɢ Lᴜᴏ,[1,2] Zᴀᴄʜᴀʀʏ L. Nᴇᴡᴍᴀɴ,[3]
Gʀɪsʜᴀ Sᴘᴇᴋᴛᴏʀ,[1,2] Jᴜɴʏᴇᴏʙ Sᴏɴɢ,[4] Oᴋᴀɴ Kᴏᴋsᴀʟ,[4] Aᴋᴀsʜ V. Rᴀᴋʜᴏʟɪᴀ,[5]
Wɪʟʟɪᴀᴍ Lᴜɴᴅᴇɴ,[5] Dᴀɴɪᴇʟ Sʜᴇʀᴇᴅʏ,[5] Pᴀʀᴛʜ B. Pᴀᴛᴇʟ,[5] Mᴀʀᴛɪɴ M. Bᴏʏᴅ,[5] Wᴇɴqɪ Zʜᴜ,[4]
Aᴍɪᴛ Aɢʀᴀᴡᴀʟ,[4] Tʀᴀᴠɪs C. Bʀɪʟᴇs,[1] ᴀɴᴅ Sᴄᴏᴛᴛ B. Pᴀᴘᴘ[1,2,*]

[1] *Time and Frequency Division, National Institute of Standards and Technology, Boulder, Colorado 80305, USA*
[2] *Department of Physics, University of Colorado, Boulder, Colorado 80309, USA*
[3] *Octave Photonics, Louisville, Colorado 80027, USA*
[4] *Microsystems and Nanotechnology Division, National Institute of Standards and Technology, Gaithersburg, Maryland 20899, USA*
[5] *Vector Atomic, Inc., Pleasanton, California 94588, USA*
*scott.papp@nist.gov

We demonstrate the formation of a complex, multi-wavelength, three-dimensional laser beam configuration with integrated metasurface (MS) optics. Our experiments support the development of a compact Sr optical-lattice clock, which leverages magneto-optical trapping at 461 nm and 689 nm without bulk free-space optics. We integrate six mm-scale metasurfaces on a fused silica substrate and illuminate them with light from optical fibers. The metasurfaces provide full control of beam pointing, divergence, and polarization to create the laser configuration for a magneto-optical trap. We report the efficiency and integration of the visible laser beam configuration, demonstrating the suitability of metasurface optics for atomic laser cooling.

Laser-cooled gases of alkaline-earth atoms have led to revolutionary advances in atomic clocks and precision measurement [1]. The magneto-optical trap (MOT), which consists of three pairs of intersecting laser beams and a magnetic quadrupole field, has been the dominant method of preparing ultracold atomic vapors since its invention decades ago. In a research laboratory, MOTs for alkaline-earth atoms are typically built from an array of optical components that must be carefully aligned, taking up a volume of ~ 1 m³. This level of complexity is a significant barrier to the development of portable cold atom systems that can address applications in geodesy and inertial sensing. In particular, integrated MOTs would greatly benefit the development of compact optical-lattice clocks based on the ultra-narrow, spin-forbidden $^1S_0 \rightarrow {}^3P_0$ transition in ^{87}Sr and other alkaline-earth systems [1]. Recently, there has been a push toward using micro- or nanofabricated integrated photonic systems [2] that are compatible with foundry-scale manufacturing, leading to a reduction in MOT size by orders of magnitude, as well as decreased complexity and cost.

Compared to alkali atoms such as rubidium, strontium poses challenges to any photonic integration for MOTs. The broad linewidth of the $^1S_0 \rightarrow {}^1P_1$ cooling transition at 461 nm and the lack of sub-Doppler cooling mechanisms require a second stage MOT on the narrow $^1S_0 \rightarrow {}^3P_1$ transition at 689 nm to reach µK temperatures. Previous work on integrated Sr MOTs with pyramid reflectors has suffered from limited optical access to the atom cloud [3]. The planarized geometry of grating MOTs [4] addresses this problem, but such systems are unable to achieve the level of precise beam control found in traditional MOTs built from bulk optics. This limitation is problematic when cooling atoms with complex level structures such as ^{87}Sr [5]. An alternative integration approach is to use metasurface (MS) optics that consist of periodic arrays of dielectric nanopillars [6]. These devices are capable of flexible control of the optical phase and offer the potential to perform the function of multiple traditional optics simultaneously in a single wafer-thickness optic. To date, atom trapping experiments with MSs have underutilized their multifunctional capabilities and have required auxiliary optical components to achieve the necessary level of control. Furthermore, the demonstrated MS beam delivery methods represent significant challenges to creating scalable systems. Free-space coupled MS systems [7–9] still require optical alignment and assembly, while guided mode approaches using photonic integrated circuits (PICs) [10–12] exhibit high-propagation loss of distances of ≈ 10 mm, especially at the visible wavelengths necessary to trap Sr [13].

Here, we demonstrate the multi-wavelength integration of metasurface optics on a common substrate to generate the laser beam configuration for a Sr laser cooling at 461 nm and 689
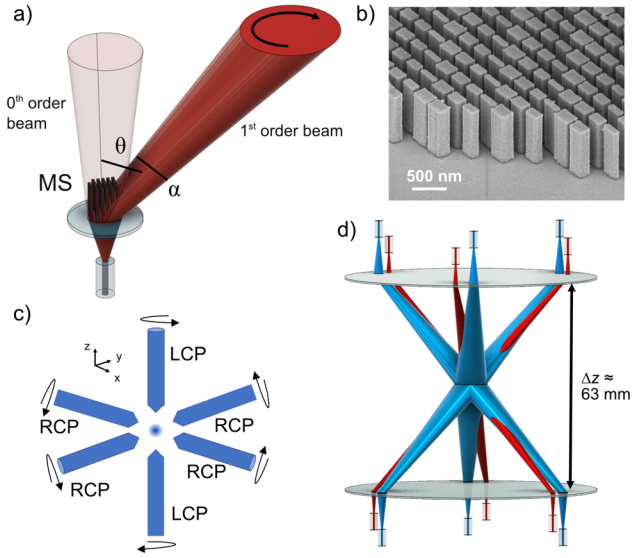
Fig. 1. Metasurface (MS) functionality and their integration for two-stage Sr MOTs. (a) Each MS controls the beam deflection angle θ, full divergence angle α, and the circular polarization state. (b) SEM image of the MS. (c) Beam geometry and polarization in a conventional cubic MOT. (d) Multi-wavelength MS integration on fiber-coupled, 3-in. wafers to produce all 12 trapping beams for 461-nm and 689-nm MOTs.

nm. Our metasurface optics platform enables the generation of the complete beam configuration of a MOT using two such substrates and the light emitted by optical fibers without any bulk free-space optics. Additionally, our foundry-compatible integration strategy avoids the high-propagation loss found in PIC approaches and eliminates the need for assembly and optical alignment required for traditional MOTs. Instead, these features are automatically incorporated into our design at the nanophotonic level by integrating multiple functionalities into a single MS optic and at the system level by integrating MS designs for different beams and wavelengths on semiconductor wafers. Each MS simultaneously performs the beam formation functions of conventional steering mirrors and lenses, as well as the polarization transformation of quarter-wave plates (QWPs). We present a comprehensive characterization of the design and performance of our nanofabricated structures, underscoring their potential role as building blocks in future integrated, nanophotonic optical systems for diverse applications in cold atom quantum computing and quantum sensing.

Figure 1 introduces our metasurface optics devices and describes how we use them as compact replacements for traditional MOT optics. The basis for beam control with MSs is the spatially dependent phase shift that results from the interaction of the optical beam with nanopillars of specific sizes placed across the transverse x–y plane [6]. We set the size and distribution of the nanopillars to design a polarization-dependent MS phase function that transforms the linearly polarized input optical mode from an optical fiber into a first-order beam deflected by angle θ with efficiency η, focused to full divergence angle α, and circularly polarized to ellipticity angle χ; see Fig. 1(a). The first-order output beam is used for trapping, but we note a residual, undeflected zeroth-order beam.

The MS transforms the phase of the input beam according to the following:

$$\phi(x, y) = k_0 x \sin(\theta) + k_0 \left(|f_1| - \sqrt{x^2 + y^2 + f_1^2} \right)$$
$$+ k_0 \left(\sqrt{x^2 + y^2 + f_2^2} - |f_2| \right), \tag{1}$$

where $k_0 = \frac{2\pi}{\lambda}$ and λ is the design wavelength. We implement the phase map given by Eq. (1) by wrapping the phase between 0 and 2π. The first term in Eq. (1) represents the grating-like deflection at our designed angle of $\theta = \pi/4$, and the last two terms represent a superposition of focusing lenses with focal length f_i that controls the beam shape. f_1 is a convex lens used to collimate the fiber input mode, and f_2 is a concave lens that controls the beam divergence angle α. The birefringent properties of our MS originate in the designed asymmetry in the nanopillars' transverse dimensions, L_x and L_y; refer to the SEM image in Fig. 1(b). To obtain beams with circular polarization, we choose a subset of pillars that results in a fixed quarter-wave phase lag between the two orthogonal components of the electric field, analogous to the fast and slow axes in a QWP. This amounts to computing the phase shifts for light linearly polarized along $\hat{x}$ (ϕ_x) and $\hat{y}$ (ϕ_y) and determining which pillars satisfy $\phi_x = \phi_y + \pi/2$. Our MSs produce left circular polarization (LCP) when the input field is polarized along an azimuthal angle between L_x and L_y of $\beta_{\text{in}} = \pi/4$ and right circular polarization (RCP) for $\beta_{\text{in}} = -\pi/4$ where β_{in} is measured from L_x.

Our MSs are composed of TiO$_2$ nanopillars arranged on a grid of periodicity $p = 220$ nm (330 nm) for a wavelength of 461 nm (689 nm) with (L_x, L_y) varying from 0.3 p to 0.8 p; an SEM image of a sample MS is shown in Fig. 1(b). We chose a pillar height of 900 nm to allow for efficient MS designs at each cooling wavelength to be integrated on a single, 0.5-mm-thick fused silica wafer. The nanostructures are fabricated using a damascene process [14], which allows for the definition of high-aspect-ratio features. We use electron-beam lithography (EBL) to form 900-nm deep holes in a resist layer that is subsequently filled with atomic layer deposition of TiO$_2$. The film is planarized with an etch step and the resist layer is removed with lift-off leaving isolated TiO$_2$ pillars.

Our trapping beam geometry resembles the conventional MOT shown in Fig. 1(c) but is modified to enable the generation of three beams for each wavelength from a single wafer and all 12 beams from two wafers; see Fig. 1(d). We create counterpropagating beams that are circularly polarized with the same handedness (LCP or RCP) relative to fixed lab coordinates to appropriately drive the $\sigma^{\pm}$ transitions in the atoms and direct the atoms toward the center of the trap. The diameter, d, divergence angle α, and power P_{MOT} of the beams are chosen to give the desired trapping volume and to efficiently cool atoms from our thermal oven source based on the saturation intensity for each transition as well as the available fiber-coupled laser power, P_{fiber}. Our system is designed to achieve a total beam intensity of 33 mW/cm^2 and 42 mW/cm^2 for the 461-nm and 689-nm transitions respectively.

Figure 2 presents our characterization of the 461-nm and 689-nm MSs for the three functionalities outlined in Fig. 1(a). We first analyze the polarization transformation of the first-order beam through polarimeter measurements of the degree of circular polarization, *DOCP*, as a function of the input azimuthal
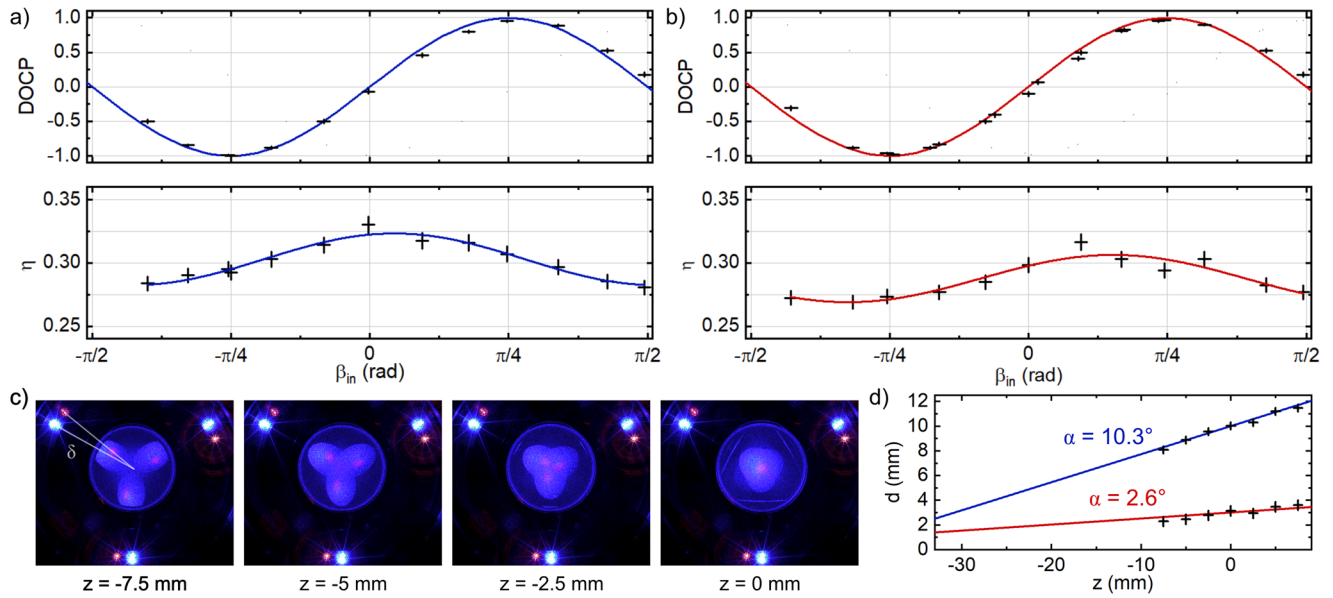
Fig. 2. Characterization of MS beams. (a) and (b) show the degree of circular polarization, *DOCP*, (top) and deflection efficiency, η, (bottom) versus input linear polarization angle, β_{in}, for 461 nm and 689 nm, respectively. (c) Images of the 461-nm (blue) and 689-nm (red) beams at various heights z showing a common intersection at $z = 0$. The angular separation of the MSs on the wafer, δ, is evident in the undeflected, zeroth-order beams. (d) Measured beam widths versus z and comparison to the expected trend of our design values for $\alpha = 10.3°$ (461 nm) and $\alpha = 2.6°$ (689 nm). The error bars in (a)–(d) are instrumental uncertainty at 95% confidence.

polarization angle, β_{in}. For our fully polarized beams, *DOCP* represents the fraction of the optical power that is circularly polarized. It is defined using the third Stokes parameter (S_3) so that $DOCP = S_3 = \sin 2\chi$. $DOCP = -1$ corresponds to LCP and $DOCP = +1$ to RCP. Measurements at 461 nm and 689 nm are shown in the top panels of Figs. 2(a) and 2(b), respectively; the error bars are instrumental uncertainty at 95% confidence. The equivalent QWP for our system produces a beam with ellipticity angle $\chi_{\text{out}} = \beta_{\text{in}}$ from which we calculate the theoretical behavior $DOCP = \sin 2\beta_{\text{in}}$. Our MSs reproduce this relation (blue and red lines) across the complete range of input angles and reach $|DOCP| \geq 0.95$ for both LCP and RCP at each wavelength.

Balanced optical powers in the counterpropagating beams are important for achieving balanced scattering forces and a stable MOT operation. We investigate the sensitivity of the beam power to misalignments in β_{in} through measurements of the effective deflection efficiency defined as $\eta = P_{\text{MOT}}/P_{\text{fiber}}$. We measure $\eta \approx 30\%$ (28.5%) at 461 nm (689 nm), respectively, for both LCP and RCP and observe a weak sinusoidal dependence on the input polarization angle; see bottom panels of Figs. 2(a) and 2(b) for data and fits. We attribute the modulation to slightly different transmission for light polarized along $\hat{x}$ and $\hat{y}$. η is affected by a non-ideal overlap between the fiber mode and finite-sized MS. When these effective aperture effects are taken into account, we find a fundamental MS efficiency of $\approx 45\%$ which is in good agreement with results from our simulations. These measurements indicate that the dominant effect of the misaligned polarization is to alter *DOCP* and minimally affect η.

To reliably define the trapping volume and beam intensity, different MSs must generate beams with consistent orientations ($\theta = 45°$) and shapes (α). We characterize these parameters by imaging the beams on a ground glass substrate at different heights above the wafer and performing routine image analysis to determine the beam positions and widths. Figure 2(c) shows the images of the beams generated by a single wafer at various heights. All six beams come to an intersection at the trap center located at the midpoint between the wafers; see far

right panel for relative height $z = 0$. Figure 2(d) shows the single beam measurements of the beam diameter with instrumental error bars. At 461 nm (689 nm), we see excellent agreement with the expected trend shown as a blue line (red line) for the designed divergence angles of $\alpha = 10.3°$ ($\alpha = 2.6°$) and diameter at the trap center, $d = 10$ mm ($d = 3$ mm).

Figure 3 presents the system-level integration of our photonics with our compact vacuum chamber and magnetic field coils for a dual-color Sr MOT; see Fig. 3(a) for a three-dimensional mechanical drawing. The 461-nm and 689-nm MSs are laid out on the wafer in a circle of radius R with an azimuthal separation of $2\pi/3$; see Fig. 3(b,i) for a diagram of the top wafer as viewed from the trap center. We use elliptically shaped MSs with semi-major (A) and semi-minor (B) radii related by $A = \sqrt{2}B$ to achieve a circular beam cross section after being deflected by $\theta = \pi/4$. While larger MSs would increase η, we choose a 461-nm (689-nm) major diameters of $2A = 2.8$ mm (1.4 mm) based on the <8 h, whole-wafer EBL write-time. We label the MS devices on the top (bottom) wafer by T_i (B_i) where the index $i = 1, 2, 3$ describes the MS location counting clockwise starting with the device opposite the wafer flat. The $i = 1$ devices generate the "axial beams" that pass through both magnetic field coils with a direction of propagation (blue and red arrows) that is approximately parallel to the direction of the strongest magnetic field gradient, $\nabla|\mathbf{B}|$ (black arrow). The top and bottom wafers differ only in the choice of δ and a mirror flip along the wafer midline parallel to the wafer flat. This results in the desired counterpropagating beam geometry when both wafers are mounted with their flats oriented opposite each other. The distance between the wafers is set with precision mounts to be $\Delta z = 2R + \epsilon$ where ϵ corrects for a small angular beam deviation in the vacuum chamber windows (refractive index $n \approx 1.52$, 2.54 mm thick).

Our MS fiber coupling strategy robustly generates beams with the desired diameter at the trap center in a compact, plug-and-play package. We offset the 689-nm and 461-nm devices by
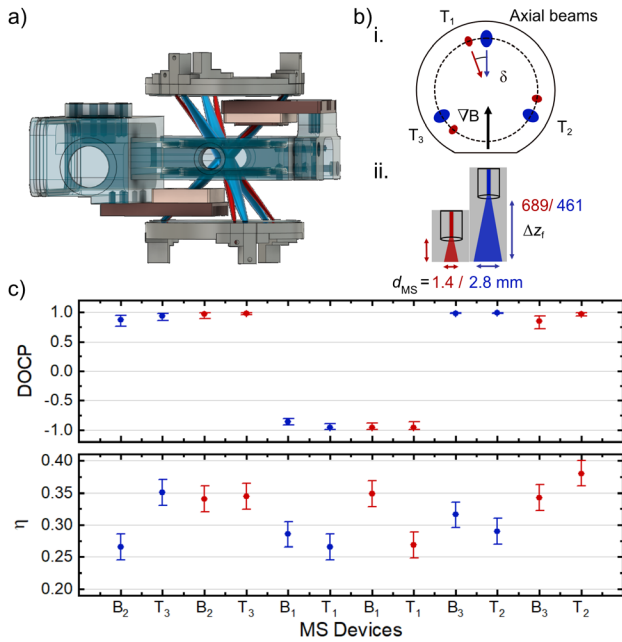
Fig. 3. System-level integration. (a) CAD drawing showing two wafers mounted over our vacuum chamber and magnetic field coils. (b,i) 461-nm (blue ovals) and 689-nm MSs (red ovals) are laid out on the wafer with a minimal separation δ to maintain orientation with respect to $\nabla|\mathbf{B}|$. (b,ii) Fiber fixtures that mechanically set the mode diameter at the MS, d_{MS}. (c) *DOCP* (top) and η (bottom) measurements for all 12 MSs.

an angle of δ to allow for the inclusion of compact, LC fiber connectors. Our choice of $\delta = -10°$ $(+10°)$ for the top (bottom) wafer is sufficiently small to ensure that the 689-nm beams approximately maintain the geometry of the 461-nm beams with respect to $\nabla|\mathbf{B}|$. We note that the lateral offset between our magnetic field coils and non-cubic propagation angle $\theta = \pi/4$ means that neither wavelength experiences the traditional projections along $\nabla|\mathbf{B}|$ for a cubic MOT. We manually rotate the fiber ferrule into the keyless fixture to set the input polarization to generate LCP or RCP as desired. This step represents the only manual alignment in our system, but we note that a small alignment key could be included in future systems. We achieve the desired trapping beam diameter through control of f_i in the second term in Eq. (1) and the $1/e^2$ diameter of the optical mode incident on the MS, d_{MS}. To minimize aperture losses due to finite MS size, we set $d_{MS} = 2A$. The fibers that deliver the 461-nm (PM-S405-XP) and 689-nm (PM630-HP) light have similar NAs and divergence angles so that d_{MS} is primarily controlled by the distance between the fiber and MS, Δz_f; see Fig. 3(b,ii). We set $\Delta z_f = 16$ mm at 461 nm and $\Delta z_f = 7.3$ mm at 689 nm. We also tightly control the lateral alignment between the optical fiber and the MS using high tolerance mechanical components to prevent errors in the beam-pointing direction that arise from off-axis coupling to the MSs. These effects are most consequential for small-diameter beams where a small shift in position can lead to a large reduction in fractional overlap at the intersection volume. For the 689-nm beams with a diameter of 3 mm at the trap center, a 140-μm error in the position of the fiber core can lead to a 50% reduction in the overlap at the trap center for two counterpropagating beams. To achieve this, the location of each 1.25-mm diameter ferrule in the fiber fixture is defined with a precision drilled hole and secured with a set screw.

Finally, we evaluate the system-level performance of our MSs when used with COTS fiber components. Figure 3(c) shows measurements of the average $(DOCP, \eta)$ that can be obtained over reasonable misalignments of the input polarization; error bars represent instrumental uncertainty at 95% confidence. MS devices at 461 nm (689 nm) are grouped according to pairs of counterpropagating beams (e.g., B_2 and T_3) and displayed as blue (red) circles. The $i = 1$ axial beams are set to LCP ($DOCP = -1$) and the $i = 2, 3$ beams to RCP ($DOCP = +1$). Some of the devices shown have lower polarization purity than the $|DOCP| \geq 0.95$ level observed in Fig. 2. This reduction in $|DOCP|$ is caused by the non-ideal performance of our visible PM fibers that are especially susceptible to misalignments of PM stress rods when using FC/APC connections. This misalignment results in a small degree of elliptical polarization at the output of the fiber (input to MS) that cannot be suppressed by azimuthal rotations of the ferrule to set β_{in}. Nevertheless, we find $|DOCP| \geq 0.85$ for devices in our system, which is sufficient for trapping [15]. As expected, η is minimally affected by improper input polarization, and we obtain an average efficiency across all beams of $\eta_{avg} = 30 \pm 3\%$ at 461 nm and $33 \pm 4\%$ at 689 nm (bottom panel); here the uncertainty range represents the statistical uncertainty at 65% confidence.

In conclusion, our work demonstrates the successful multi-wavelength integration of six mm-scale metasurface optics on a single substrate to create a complex configuration of laser beams for optical cooling of Sr at 461 nm and 689 nm. Our multifunction metasurface optics achieve precise control over beam pointing, divergence, and polarization state without the need for bulk free-space optics.

Disclosures. The authors declare no conflicts of interest.

Data availability. Data underlying the results presented in this paper are not publicly available but may be obtained from the authors upon reasonable request.

REFERENCES

1. A. D. Ludlow, M. M. Boyd, J. Ye, *et al.*, Rev. Mod. Phys. **87**, 637 (2015).
2. J. P. McGilligan, K. Gallacher, P. F. Griffin, *et al.*, Rev. Sci. Instrum. **93**, 091101 (2022).
3. W. Bowden, R. Hobson, I. R. Hill, *et al.*, Sci. Rep. **9**, 11704 (2019).
4. A. Sitaram, P. K. Elgee, G. K. Campbell, *et al.*, Rev. Sci. Instrum. **91**, 103202 (2020).
5. D. S. Barker, P. K. Elgee, A. Sitaram, *et al.*, New J. Phys. **25**, 103046 (2023).
6. A. Arbabi and A. Faraon, Nat. Photonics **17**, 16 (2023).
7. L. Zhu, X. Liu, B. Sain, *et al.*, Sci. Adv. **6**, eabb6667 (2020).
8. W. R. McGehee, W. Zhu, D. S. Barker, *et al.*, New J. Phys. **23**, 013021 (2021).
9. T. W. Hsu, W. Zhu, T. Thiele, *et al.*, PRX Quantum **3**, 030316 (2022).
10. A. Yulaev, W. Zhu, C. Zhang, *et al.*, ACS Photonics **6**, 2902 (2019).
11. G. Spektor, D. Carlson, Z. Newman, *et al.*, Optica **10**, 871 (2023).
12. A. Isichenko, N. Chauhan, D. Bose, *et al.*, Nat. Commun. **14**, 3080 (2023).
13. C. Ropp, W. Zhu, A. Yulaev, *et al.*, Light: Sci. Appl. **12**, 83 (2023).
14. Q. Fan, M. Liu, C. Zhang, *et al.*, Phys. Rev. Lett. **125**, 267402 (2020).
15. A. R. Ferdinand, Z. Luo, S. Jammi, *et al.*, "Laser cooling ^{88}Sr to microkelvin temperature with an integrated-photonics system," arXiv (2024).